

SPRig: Self-Supervised Pose-Invariant Rigging from Dynamic Mesh Sequences

Ruipeng Wang^{1*}, Langkun Zhong^{2**}, and Miaowei Wang³

¹ University of Pennsylvania, Philadelphia, USA
ruipeng@sas.upenn.edu

² The University of Hong Kong, Hong Kong, China
zhong_langkun@outlook.com

³ The University of Edinburgh, Edinburgh, UK
s2608314@ed.ac.uk

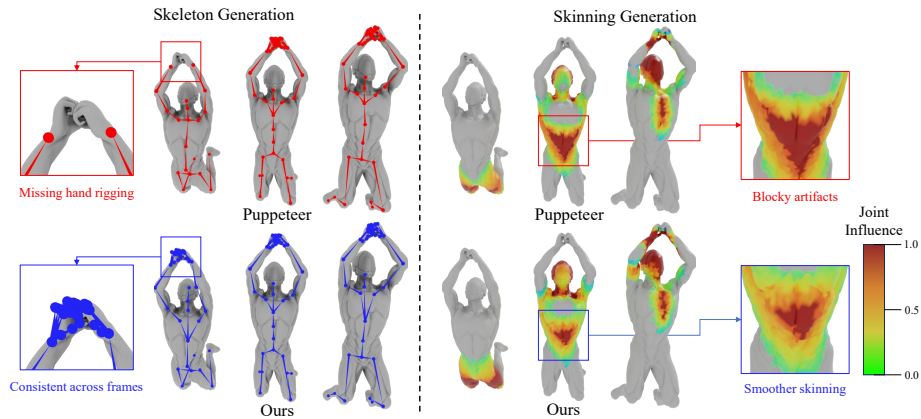


Fig. 1: We propose **SPRig**, a fine-tuning framework that enforces cross-frame consistency to learn pose-invariant rigs on existing models. It generates more consistent skeletons and smoother, stable skinning across frames, outperforming static methods such as Puppeteer [65]. See the supplementary video for full dynamics.

Abstract. State-of-the-art rigging methods typically assume a predefined canonical rest pose. However, this assumption does not hold for dynamic mesh sequences such as DyMesh or DT4D, where no canonical T-pose is available. When applied independently frame-by-frame, existing methods lack pose invariance and often yield temporally inconsistent topologies. To address this limitation, we propose **SPRig**, a general fine-tuning framework that enforces cross-frame consistency across a sequence to learn pose-invariant rigs on top of existing models, covering both skeleton and skinning generation. For skeleton generation, we introduce novel consistency regularization in both token space and geometry space. For skinning, we improve temporal stability through an

* Equal contribution

** Equal contribution

articulation-invariant consistency loss combined with consistency distillation and structural regularization. Extensive experiments show that SPRig achieves superior temporal coherence and significantly reduces artifacts in prior methods, without sacrificing and often even enhancing per-frame static generation quality. The code is available in the supplemental material and will be made publicly available upon publication.

Keywords: Automatic rigging · Pose invariance · Temporal consistency

1 Introduction

3D character rigging, which encompasses skeleton [10] and skinning [36] tuning, remains a fundamental yet time-consuming bottleneck in modern content creation pipelines for games [30], film [29], and virtual reality [48].

Therefore, many automatic rigging tools [7, 12, 13, 24, 25, 37, 41, 42, 44, 54, 68, 70, 71, 88] have been developed to accelerate this process. Early automatic rigging methods [4] relied on geometric heuristics and template fitting, which often struggled to generalize across diverse topologies. With the rise of deep learning [35], RIGNET [81] reframed rigging as a learning-based task. More recently, state-of-the-art (SOTA) methods [65, 94] have achieved substantial improvements by leveraging powerful Transformer-based [75] autoregressive models [60], to generate high-quality rigs.

However, these SOTA models are primarily designed for static inputs, specifically requiring a standard T-pose (a standardized neutral posture) for initialization. This assumption is fundamentally incompatible with modern dynamic mesh sequences [38, 45, 80], including human-designed synthetic animations [17, 19], dynamic 3D generative models [76, 80], 4D video reconstructions [22, 64, 85], and real-world 4D scanning captures [8, 15], which typically lack a fixed canonical reference, either because none is provided or because no corresponding natural pose exists. When applied frame-by-frame independently, these models lack temporal consistency and fail to preserve structural coherence across the sequence. This failure manifests as severe visual artifacts, most notably topological flickering and erratic changes in surface connectivity between frames (Fig. 1, Top).

Addressing temporal inconsistency is essential: flickering rigs disrupt animation pipelines and require tedious manual cleanup. Although static rigging datasets are abundant, high-quality labeled dynamic datasets with skeletons and skinning are scarce, necessitating supervision directly from the sequence. Our key insight, rooted in a fundamental graphics principle, is that an animated sequence represents a single object and should have a single, pose-invariant rig. We exploit this as a self-supervised signal: a canonical rig from an anchor frame guides fine-tuning of a pre-trained frame-by-frame model, enforcing consistency across the sequence.

We propose **SPRig**, a novel fine-tuning framework built upon a frozen-teacher and trainable-student paradigm. In this setup, a frozen pre-trained model (the teacher) infers a high-quality rig on a single canonical anchor frame. This prediction then serves as a pose-invariant target to supervise a trainable

copy (the student) across all other dynamic frames. By exploiting this self-supervised signal from unlabeled animated mesh sequences, SPRig injects temporal consistency into pretrained static rigging models, making them significantly more robust to pose variations. Specifically, SPRig applies this anchor-based strategy at two stages. For skeleton generation stage, we couple autoregressive token-space constraints with a geometry-space loss that utilizes rigid Procrustes alignment [74] to decouple global motion, forcing the model to replicate the anchor’s topology regardless of pose. For skinning generation stage, we establish dense cross-frame correspondences via barycentric tracking, and apply consistency distillation modulated by a soft-support mask to filter out teacher noise. This is further regularized by entropy and geometric proximity priors to guarantee sharp, physically plausible joint assignments.

Extensive experiments show that our method produces high-quality rigs across dynamic mesh sequences [38, 80] while maintaining and even improving per-frame static rigging performance on challenging out-of-domain datasets.

In summary, our contributions are as follows:

- SPRig, a self-supervised fine-tuning framework that enhances temporal stability and pose-invariance in SOTA models using only unlabeled sequences.
- A set of dual consistency losses for learning pose-invariant skeleton topology and coherent skinning across dynamic mesh frames.

2 Related Work

Static automatic rigging. Early automatic rigging relied on geometric heuristics and template fitting [1, 3, 4, 6, 9, 21, 28, 51, 53, 55, 56, 72, 73, 83, 84]. PINOCCHIO [4] depends strongly on template quality and struggles with novel topologies. To improve generalization, the field shifted to data-driven approaches. RIGNET [81] framed rigging as an end-to-end learning problem, and subsequent models trained on large artist-created datasets [18, 20, 39, 96] showed strong generalization. With Transformers succeeding in 3D generation [40, 57, 79, 89, 91, 92, 97, 98], recent SOTAs adopt autoregressive decoding frameworks. Specifically, UNIRIG [94] formulates rigging as a discrete token sequence generation task, while PUPPETEER [65] scales up this autoregressive paradigm with a larger model capacity and a significantly expanded, highly diverse training dataset. For skinning, these modern methods typically leverage cross-attention between surface points and bones to robustly assign joint influences. While these methods excel on static assets, they are fundamentally non-temporal. Applying them independently to dynamic sequences leads to severe frame-to-frame inconsistencies (e.g., joint drift, topology flicker) that we target in this work.

Rigging from dynamic sequences and 4D reconstruction. A parallel line of research [2, 16, 27, 31, 34, 47, 50] extracts rigging or motion directly from sequential data. Recent advances extend this to diverse inputs: MORIG [82] extracts motion-aware features to rig 3D point cloud sequences, LASR [85] recovers articulated shape and kinematics directly from monocular video via differentiable

rendering, and REACTO [67] reconstructs articulated neural implicit representations by tracking dense correspondences from casual videos (along with others [62, 66, 69, 78, 86, 87, 93, 99]). Concurrently, the rapid development of dynamic 3D mesh reconstruction and generation [8, 11, 80, 90] has made high-quality, in-the-wild mesh sequences increasingly obtainable. However, these sequences are typically unlabeled (lacking ground-truth skeletons or skinning). Rather than training a model from scratch to extract rigs from these sequences, SPRIG takes a novel perspective: we utilize these abundant, unlabeled dynamic mesh sequences as the perfect self-supervised signal. By enforcing temporal continuity across the sequence, we fine-tune and stabilize the aforementioned static foundation models, marrying powerful static generalization with strict dynamic coherence.

3 Methodology Overview

Given an animated mesh sequence $\mathcal{M} = \{\mathbf{M}^k\}_{k=1}^K$ with consistent vertex correspondences, we seek a temporally consistent rig: a skeleton stable in both joint positions and kinematic topology across all frames (Stage 1, Sec. 4), together with skinning weights that assign each surface point consistently to the same set of joints across all poses (Stage 2, Sec. 5).

Core principle. Both stages share the same teacher–student design [26]: a *frozen* pretrained model (teacher) produces a high-quality prediction on anchor frame c only; a *trainable* copy (student) is fine-tuned so that its output on every frame k matches that anchor prediction, yielding pose-invariant results without retraining from scratch.

Anchor frame. Both stages are grounded in a single canonical frame c , selected automatically using a geometric criterion. Our key observation is that the most articulation-free and topologically explicit pose—typically resembling a T-pose—maximizes the exposed surface area. Rather than using the conventional first frame [16], which may suffer from self-occlusions or curled configurations, we search for the most extended pose in the sequence. For each frame \mathbf{M}^k , we compute its total surface area $\mathcal{A}(\mathbf{M}^k)$ (sum of triangle areas) and select $c = \arg \max_k \mathcal{A}(\mathbf{M}^k)$ as the anchor frame. This frame provides a stable canonical reference that reduces the risk of degenerate joint configurations, and then all meshes are normalized using its axis-aligned bounding box.

Notation. We use J joints and K frames. A skeleton is a pair $(\mathbf{X}^k \in \mathbb{R}^{J \times 3}, \mathbf{P}^k \in \{0, \dots, J\}^J)$ of joint positions and parent indices. We denote $\mathbf{x}_j^k := [\mathbf{X}^k]_j$ and $p_j^k := [\mathbf{P}^k]_j$ as the j -joint’s position and kinematic parent respectively, where $p_j^k = 0$ indicates the root. The anchor skeleton $(\mathbf{X}^c, \mathbf{P}^c)$ from skeleton generation (Stage 1) is passed as conditioning input to skinning generation (Stage 2). We write $\mathcal{K} := \{k \mid k \neq c, k \in \{1, \dots, K\}\}$ for the non-anchor frame set.

4 Skeleton Generation

Autoregressive skeleton decoders [65, 68, 94, 95] represent a skeleton as a discrete token stream encoding both geometry and kinematic topology. While effective

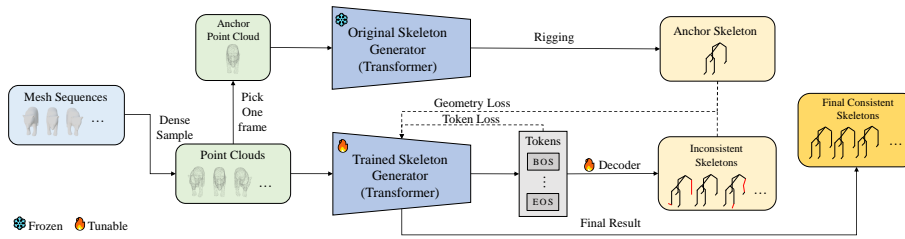


Fig. 2: Skeleton generation overview. Point clouds sampled from the mesh sequence are processed by a shared skeleton generator. The frozen teacher takes only the anchor frame c and produces a canonical token sequence. This sequence is provided as a prefix to the student at every frame. The student is then fine-tuned with token-level and geometry-level consistency losses to generate temporally stable skeletons.

for single-frame prediction, they suffer from temporal inconsistency: minor shape variations across frames can induce different tokenizations, manifesting as re-parenting events and positional jitter [59]. The root cause is that each frame is decoded independently, with no cross-frame consistency mechanism.

We address this with the teacher–student framework (Fig. 2). The frozen teacher processes anchor frame c to generate a stable reference skeleton and token sequence. The trainable student is fine-tuned across all K frames via two consistency losses: token space (Sec. 4.2) and geometry space (Sec. 4.3), driving its outputs to match the anchor reference regardless of pose.

4.1 Tokenization

Teacher and student share the same autoregressive decoder G_θ , which operates on per-frame features \mathbf{F}^k extracted from area-weighted random points [52] sampled from mesh \mathbf{M}^k . Given \mathbf{F}^k , the decoder generates a token sequence $\mathbf{t}^k = \{t_i^k\}_{i=1}^L$, $L = 4J$, factorizing as $p_\theta(\mathbf{t}^k | \mathbf{F}^k) = \prod_{i=1}^L p_\theta(t_i^k | t_{<i}^k, \mathbf{F}^k)$.

Tokens \mathbf{t}^k are organized into per-joint quadruples $\{(t_{j,x}^k, t_{j,y}^k, t_{j,z}^k, t_{j,p}^k)\}_{j=1}^J$. The coordinate tokens $t_{j,x}^k, t_{j,y}^k, t_{j,z}^k \in \{1, \dots, B\}$ encode uniformly quantized Cartesian coordinates in a normalized bounding box, with B bins. The parent token $t_{j,p}^k \in \{0, \dots, J\}$ encodes the parent index p_j^k , with $t_{j,p}^k = 0$ indicating the root. At inference, projecting \mathbf{t}^k yields the skeleton $(\mathbf{X}^k, \mathbf{P}^k)$.

4.2 Token Consistency

The objective is to make the student approximate the teacher’s anchor token sequence on every frame. Under *teacher forcing* [5, 77], the student at each step i receives the anchor prefix $t_{<i}^c$ rather than its own past outputs, decoupling predictions from its own accumulated errors. Parent tokens $\{t_{j,p}^k\}$ occupy position $4j$ (1-indexed) of joint j ’s quadruple.

Self-anchor loss (frame c). On frame c , we minimize the weighted cross-entropy between the student’s predicted logits z_i^c and the teacher’s hard token labels \hat{t}_i^c :

$$\mathcal{L}_{\text{self}} = \frac{\sum_i w_i \text{CE}(z_i^c, \hat{t}_i^c)}{\sum_i w_i}, \quad (1)$$

where w_i is empirically set to 5 for parent tokens to prioritize global topological stability and $w_i = 1$ otherwise.

Cross-frame loss ($k \in \mathcal{K}$). The student receives pose-specific features \mathbf{F}^k but is prefixed with the anchor sequence $\hat{t}_{<i}$, driving its outputs to approximate the canonical token sequence regardless of pose variations across frames:

$$\mathcal{L}_{\text{cross}} = \frac{1}{K-1} \sum_{k \in \mathcal{K}} \frac{\sum_i w_i \text{CE}(z_i^{c,k}, \hat{t}_i^c)}{\sum_i w_i}. \quad (2)$$

The combined token objective $\mathcal{L}_{\text{token}} = \lambda_{\text{anc}} \mathcal{L}_{\text{anc}} + \lambda_{\text{sym}} \mathcal{L}_{\text{sym}}$, with $\lambda_{\text{anc}}, \lambda_{\text{sym}} > 0$, trains the student to replicate the anchor token sequence from any pose.

4.3 Geometry Consistency

Token-level supervision is prone to *exposure bias* [61], where teacher forcing induces a train–test mismatch that accumulates at inference. To mitigate this, we introduce a geometry regularizer $\mathcal{L}_{\text{geom}}$ on the *projected* skeletons, designed to be invariant to global rigid transformations and joint-index permutations.

For each frame k , define bone edges $\mathcal{E}^k := \{(i, j) \mid p_j^k = i, i \neq j\}$, bone vectors $\mathbf{v}_{ij}^k := \mathbf{x}_j^k - \mathbf{x}_i^k$, and midpoints $\mathbf{m}_{ij}^k := \frac{1}{2}(\mathbf{x}_i^k + \mathbf{x}_j^k)$. We factor out global pose via rigid transform $(\mathbf{R}^k, \mathbf{T}^k)$: \mathbf{R}^k aligns inertia tensors [23] through rigid Procrustes [74], and $\mathbf{T}^k = \mu(\mathcal{M}^k) - \mathbf{R}^k \mu(\mathcal{M}^c)$, where $\mu(\cdot)$ is the centroid and $\mathcal{M}^k = \{\mathbf{m}_{ij}^k\}_{(i,j) \in \mathcal{E}^k}$. Let $\mathcal{E}_\rho^k \subseteq \mathcal{E}^k$ be the top- ρ longest edges. We measure permutation-invariant discrepancies after aligning between each frame and the anchor using three complementary terms, each targeting a distinct failure mode:

Bone direction. Without directional supervision, token errors can produce limbs pointing the wrong way. Let the normalized vector $\tilde{\mathbf{v}}_{ij}^k = \mathbf{v}_{ij}^k / \|\mathbf{v}_{ij}^k\|_2$. We define $\mathcal{L}_{c \rightarrow k} = 1 - \text{mean}_{(i,j) \in \mathcal{E}_\rho^c} \max_{(p,q) \in \mathcal{E}_\rho^k} \langle \mathbf{R}^k \tilde{\mathbf{v}}_{ij}^c, \tilde{\mathbf{v}}_{pq}^k \rangle$, and $\mathcal{L}_{k \rightarrow c}$ symmetrically. We penalizes inconsistent limb orientations with $\mathcal{L}_{\text{dir}} = \frac{1}{2}(\mathcal{L}_{c \rightarrow k} + \mathcal{L}_{k \rightarrow c})$.

Bone-length distribution. Coordinate-token quantization can cause bone lengths to drift. Let $\ell_{(r)}^k$ be the r -th edge length of frame k in ascending order and $n := \min(|\mathcal{E}^c|, |\mathcal{E}^k|)$. Then we penalize $\mathcal{L}_{\text{len}} = \frac{1}{n} \sum_{r=1}^n (\ell_{(r)}^k - \ell_{(r)}^c)^2$.

Joint endpoints. The two terms above constrain each bone independently but not their global spatial arrangement. Let $\bar{\mathbf{x}}_i^k := \mathbf{R}^k \mathbf{x}_i^c + \mathbf{T}^k$, $\mathcal{N}^k := \{[\mathbf{x}_i^k | \mathbf{x}_j^k] \in \mathbb{R}^6\}_{(i,j) \in \mathcal{E}^k}$, $\bar{\mathcal{N}}^k := \{[\bar{\mathbf{x}}_i^k | \bar{\mathbf{x}}_j^k] \in \mathbb{R}^6\}_{(i,j) \in \mathcal{E}^c}$ where $|$ denotes concatenation, and $d(A, B) := \frac{1}{|A|} \sum_{\mathbf{a} \in A} \min_{\mathbf{b} \in B} \|\mathbf{a} - \mathbf{b}\|_2^2$ (one-sided Chamfer distance). Then we design $\mathcal{L}_{\text{ch}} = \frac{1}{2}[d(\bar{\mathcal{N}}^c, \mathcal{N}^k) + d(\mathcal{N}^k, \bar{\mathcal{N}}^c)]$ to penalize endpoint mismatch.

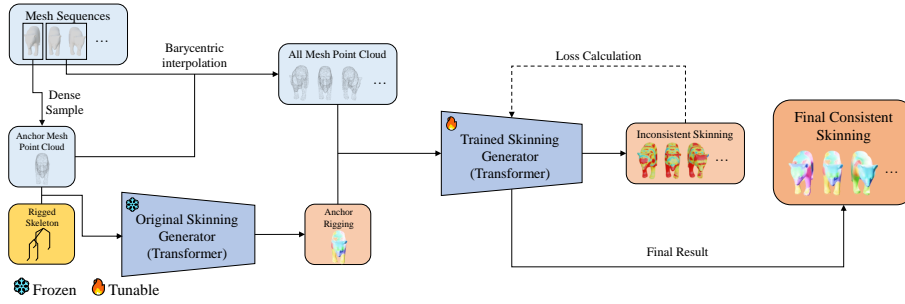


Fig. 3: Skinning generation overview. N surface points are sampled from the canonical mesh \mathbf{M}^c ; the same barycentric coordinates track those points across all frames. The frozen teacher predicts skinning weights \mathbf{W}^c on the canonical frame; the student H_ϕ is fine-tuned so that its predictions \mathbf{W}^k on every frame match \mathbf{W}^c via an articulation-invariant consistency loss.

The three terms are averaged over non-anchor frames:

$$\mathcal{L}_{\text{geom}} = \frac{1}{K-1} \sum_{k \in \mathcal{K}} (\lambda_{\text{dir}} \mathcal{L}_{\text{dir}} + \lambda_{\text{len}} \mathcal{L}_{\text{len}} + \lambda_{\text{ch}} \mathcal{L}_{\text{ch}}), \quad \lambda_{\text{dir}}, \lambda_{\text{len}}, \lambda_{\text{ch}} \geq 0. \quad (3)$$

5 Skinning Generation

Given the anchor skeleton $(\mathbf{X}^c, \mathbf{P}^c)$ from Stage 1, we seek per-point stable skinning-weight matrices $\mathbf{W}^k \in \mathbb{R}^{N \times J}$ for all frames, where each row encodes how strongly the N surface points follow each of the J joints. Naïve per-frame prediction yields inconsistent assignments across poses. We still apply the teacher-student strategy: the frozen teacher provides high-quality weights \mathbf{W}^c on the canonical frame only, which then supervises the student on all frames.

Setup. We sample N surface points from the canonical \mathbf{M}^c by triangle-area importance sampling. For each frame k , applying the same face index and barycentric coordinates to the vertices yields a pose-consistent position $[\mathbf{E}^k]_i$ for each point $i \in [1, N]$, and the corresponding normal $[\mathbf{N}^k]_i$ is obtained analogously. We stack these into $\mathbf{U}^k = [\mathbf{E}^k \mid \mathbf{N}^k] \in \mathbb{R}^{N \times 6}$. From parent index \mathbf{P}^c we derive a valid-joint mask $\mathbf{V} \in \{0, 1\}^J$, where $[\mathbf{V}]_j = 1$ iff joint $j \in [1, J]$ is a valid (non-padding) joint, and $[\mathbf{V}]_j = 0$ otherwise, and we induce unweighted shortest-path distances on the joint tree $\mathbf{D} \in \mathbb{R}^{J \times J}$; both are shared across frames.

5.1 Skinning Network

Trainable students leverage the architecture-agnostic skinning weight generator H_ϕ [65], which maps per-point queries conditioned on the anchor skeleton $(\mathbf{X}^c, \mathbf{P}^c)$ to per-point weight distributions.

$$\mathbf{W}^k = H_\phi(\mathbf{U}^k; \mathbf{X}^c, \mathbf{P}^c, \mathbf{V}, \mathbf{D}), \quad \mathbf{W}^k \in \mathbb{R}^{N \times J}, \quad (4)$$

where each row $[\mathbf{W}^k]_i \in \Delta^{J-1}$, with the simplex $\Delta^{J-1} = \{\mathbf{w} \in \mathbb{R}_{\geq 0}^J \mid \sum_j w_j = 1\}$. H_ϕ is a tri-stream Transformer processing point, joint, and shape features in parallel with topology-aware attention using \mathbf{D} (see details in Supplementary).

5.2 Canonical-Frame Teacher and Noise Suppression

The frozen teacher is run on the canonical-frame query \mathbf{U}^c to produce the distillation target:

$$\hat{\mathbf{W}}^c = H_\phi^{\text{frozen}}(\mathbf{U}^c; \mathbf{X}^c, \mathbf{P}^c, \mathbf{V}, \mathbf{D}) \in \mathbb{R}^{N \times J}. \quad (5)$$

$\hat{\mathbf{W}}^c$ is fixed and shared across all frames as the pose-invariant supervision signal.

Soft support mask. Small entries in $\hat{\mathbf{W}}^c$ reflect negligible joint influence and introduce noise. We define a soft support mask $\mathbf{S} \in [0, 1]^{N \times J}$: for each point, the top- K_s valid joints in $\hat{\mathbf{W}}^c$ receive mask value 1; remaining valid joints receive a small residual $\gamma \in (0, 1)$; padding joints are zeroed. This focuses supervision on influential joints without discarding gradient signal entirely.

We define two mask-aware operators on any weight matrix $\mathbf{A} \in \mathbb{R}_{\geq 0}^{N \times J}$: (1) *Masked renormalization* $\mathcal{R}(\mathbf{A}; \mathbf{S})$ restricts \mathbf{A} to the unmasked support:

$$\mathcal{R}(\mathbf{A}; \mathbf{S}) := \frac{\mathbf{A} \odot \mathbf{1}[\mathbf{S} > 0]}{\sum_j \mathbf{A}_{:,j} \mathbf{1}[\mathbf{S}_{:,j} > 0]} + \varepsilon, \quad (6)$$

where ε is a small constant added to prevent division by zero. (2) *Masked mean* $[\mathbf{A}]_{\mathbf{S}}$ computes the \mathbf{S} -weighted average over all point-joint pairs:

$$[\mathbf{A}]_{\mathbf{S}} := \frac{N \sum_{i,j} A_{i,j} S_{i,j}}{\sum_{i,j} S_{i,j}}. \quad (7)$$

We write $\hat{\mathbf{W}}_{\mathbf{S}}^c := \mathcal{R}(\hat{\mathbf{W}}^c; \mathbf{S})$ and $\mathbf{W}_{\mathbf{S}}^k := \mathcal{R}(\mathbf{W}^k; \mathbf{S})$ for the masked canonical teacher and student prediction, respectively.

5.3 Articulation-Invariant Skinning Consistency Loss

The student is required to reproduce $\hat{\mathbf{W}}_{\mathbf{S}}^c$ on every frame. We enforce this through *consistency distillation*, which directly matches predictions to $\hat{\mathbf{W}}_{\mathbf{S}}^c$, and *structural regularization*, which prevents degenerate solutions such as uniformly diffuse weights that minimize the distillation loss yet lack physical meaning. The total skinning consistency loss is $\mathcal{L}_{\text{skin}} = \mathcal{L}_{\text{cons}} + \mathcal{L}_{\text{reg}}$.

Consistency distillation. We align the student model’s predictions across all frames with $\hat{\mathbf{W}}_{\mathbf{S}}^c$ using a masked symmetric KL divergence [33] and a masked L_1 loss. Additionally, to prevent the student from drifting away from the anchor teacher during fine-tuning, we apply an anchor-frame loss $\mathcal{L}_{\text{anchor}}$. The combined consistency loss is $\mathcal{L}_{\text{cons}} = \lambda_{\text{sym}} \mathcal{L}_{\text{sym}} + \lambda_1 \mathcal{L}_1 + \lambda_{\text{anchor}} \mathcal{L}_{\text{anchor}}$, with weights

$\lambda_{\text{sym}}, \lambda_1, \lambda_{\text{anchor}} > 0$ controlling the relative weighting of the terms:

$$\mathcal{L}_{\text{sym}} = \frac{1}{K} \sum_{k=1}^K \left[\text{KL}(\hat{\mathbf{W}}_{\mathbf{S}}^c \parallel \mathbf{W}_{\mathbf{S}}^k) + \text{KL}(\mathbf{W}_{\mathbf{S}}^k \parallel \hat{\mathbf{W}}_{\mathbf{S}}^c) \right]_{\mathbf{S}}, \quad (8)$$

$$\mathcal{L}_1 = \frac{1}{K} \sum_{k=1}^K \left[\|\mathbf{W}_{\mathbf{S}}^k - \hat{\mathbf{W}}_{\mathbf{S}}^c\| \right]_{\mathbf{S}}, \quad (9)$$

$$\mathcal{L}_{\text{anchor}} = \left[\|\mathbf{W}_{\mathbf{S}}^c - \hat{\mathbf{W}}_{\mathbf{S}}^c\| \right]_{\mathbf{S}}. \quad (10)$$

Structural regularization. We use two teacher-independent priors to sharpen predictions: (1) The *entropy penalty* minimizes Shannon entropy [63], encouraging sparse, confident joint assignments:

$$\mathcal{L}_{\text{ent}} = - \sum_{k=0}^K \left[\mathbf{W}_{\mathbf{S}}^k \odot \log(\mathbf{W}_{\mathbf{S}}^k) \right]_{\mathbf{S}}. \quad (11)$$

(2) The *geometric proximity prior* prevents sparse and geometrically implausible assignments: a surface point should primarily follow nearby bones. For the i -th point $[\mathbf{E}^k]_i$ and j -joint’s bone $\overline{\mathbf{x}_j^c \mathbf{x}_{p_j^c}^c}$ (from Sec. 4.3), let $d_{i,j}^k$ denote the shortest Euclidean distance from the point to the segment. The exponential prior $[\mathbf{\Pi}^k]_{i,j} \propto \exp(-\beta d_{i,j}^k)$, where β is a scaling factor controlling the spatial decay rate, is averaged over a sliding window $\mathcal{W}_\tau \subset \{1, \dots, K\}$ of τ frames, we empirically set this number to 3: $\mathbf{\Pi}_{\mathcal{W}_\tau}^k = \frac{1}{\tau} \sum_{k \in \mathcal{W}_\tau} \mathbf{\Pi}^k$. The prior loss penalizes deviations from this target:

$$\mathcal{L}_{\text{prior}} = \sum_{k=1}^K \left[\text{KL}(\mathcal{R}(\mathbf{\Pi}_{\mathcal{W}_\tau}^k; \mathbf{S}) \parallel \mathbf{W}_{\mathbf{S}}^k) \right]_{\mathbf{S}}. \quad (12)$$

The structural regularization loss is $\mathcal{L}_{\text{reg}} = \lambda_{\text{ent}} \mathcal{L}_{\text{ent}} + \lambda_{\text{prior}} \mathcal{L}_{\text{prior}}$; all $\lambda_{(\cdot)} \geq 0$.

6 Experiment

Overview. We evaluate our method on two tasks: skeleton and skinning generation, aiming to make SOTA static riggers temporally stable when applied frame by frame to dynamic mesh sequences. Temporal stability is measured under an anchor-based protocol, where one frame c is selected as the canonical anchor and the others are treated as perturbed frames.

Datasets. To rigorously evaluate our method, we conduct experiments on two dynamic mesh datasets: (1) we use the standard DeformingThings4D (**DT4D**) [38] dataset, constructing a 125-sequence validation set by randomly sampling one sequence from each object category. (2) To verify that our framework scales to diverse in-the-wild topologies, we introduce a curated subset of **DyMesh** [80], comprising 1007 high-quality motion sequences with extreme deformations and varied skeletal structures.

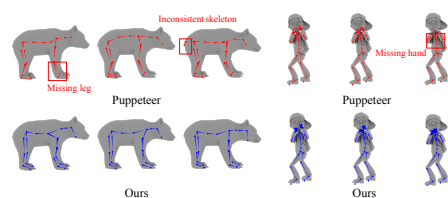


Fig. 4: Skeleton qualitative comparisons. Top (red): the Puppeteer often misses or distorts structures (e.g., missing leg on the bear and missing hand on the human), and exhibits inconsistent skeleton topology between frames. Bottom (blue): our method produces more temporally stable and complete skeletons across frames. By enforcing cross-frame consistency, SPRig effectively prevents this topological drift and preserves structural integrity within sequences.

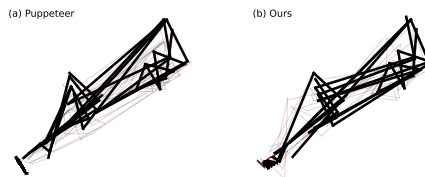


Fig. 5: Skeleton temporal jitter. To isolate structural jitter from global motion, we rigidly align all predicted skeletons in a sequence to a canonical anchor frame using Procrustes analysis. Puppeteer shows noticeable geometric jitter and inconsistent bone lengths, whereas our method learns a pose-invariant prior that keeps skeletons tightly clustered around the anchor, improving temporal stability. Thick black lines denote the canonical anchor, and thin translucent colored lines denote other frames.

Implementation Details. We instantiate SPRig by fine-tuning the pretrained Puppeteer models, though our method is agnostic to the specific Transformer architecture (see Supp. for details). Specifically, we freeze the geometry point cloud encoders and only update the Transformer decoders using self-supervised signals from the dynamically discovered canonical anchors. All experiments are implemented in PyTorch [58] and conducted on a single NVIDIA A100 GPU. We utilize the AdamW [43] optimizer for both tasks: the skeleton network is trained with a learning rate of 3×10^{-6} and a batch size of 20, while the skinning network uses a learning rate of 1×10^{-5} and a batch size of 12 with automatic mixed [49]. During fine-tuning, both models converge efficiently within 10 to 12 epochs. The entire training process takes about 20 hours to finish.

6.1 Skeleton Generation

Metrics. We report: (1) the pairwise joint distance deviation (**PJDD**), which measures geometric jitter over time by quantifying the drift in all pairwise joint distances relative to the canonical anchor after rigid alignment (see Suppl. for details); (2) **GSD** [14], which evaluates global structural consistency based on spectral graph theory. Both PJDD and GSD serve as our dynamic metrics evaluated on the DT4D and DyMesh test splits; (3) **CD-J2J**, **CD-J2B**, and **CD-B2B** [81], which serve as representative static quality metrics, which are computed on **Articulation-XL 2.0** [68], **ModelsResource** [81], and **Diverse-pose** [65] test sets for out-of-domain generalization.

Results. SPRig (see Tab. 1, Left) drastically suppresses geometric jitter compared to baselines, reducing PJDD from 17.46 to 0.68 on DT4D while main-

Table 1: Dynamic quantitative comparisons. Left: Skeleton topology generation. Right: Skinning weight generation. Our method substantially improves both skeleton and skinning metrics across DT4D and DyMesh datasets.

Model	Skeleton Generation				Skinning Generation			
	DT4D		DyMesh		DT4D		DyMesh	
	PJDD ↓	GSD ↓	PJDD ↓	GSD ↓	L ₁ Erro ↓	LBS RMSE ↓	L ₁ Error ↓	LBS RMSE ↓
UniRig	15.76	0.060	19.56	0.071	1310.31	0.007576	1430.43	0.007763
Puppeteer	17.46	0.062	16.53	0.068	1328.80	0.007560	1379.32	0.007835
Ours	0.68	0.056	0.72	0.054	982.35	0.007552	936.58	0.007447

Table 2: Skeleton static prediction comparisons. Our method maintains strong per-frame fidelity on diverse out-of-domain static datasets.

Model	Articulation-XL 2.0			ModelsResource			Diverse-Pose		
	CD-J2J ↓	CD-J2B ↓	CD-B2B ↓	CD-J2J ↓	CD-J2B ↓	CD-B2B ↓	CD-J2J ↓	CD-J2B ↓	CD-B2B ↓
UniRig	0.0331	0.0261	0.0218	0.0396	0.0302	0.0257	0.0325	0.0257	0.0208
Puppeteer	0.0311	0.0237	0.0198	0.0377	0.0280	0.0241	0.0251	0.0199	0.0160
Ours	0.0270	0.0213	0.0188	0.0325	0.0258	0.0235	0.0191	0.0178	0.0125

Table 3: Quantitative skeleton ablations. Removing the token loss ($\mathcal{L}_{\text{token}}$), geometric loss ($\mathcal{L}_{\text{geom}}$), or the hierarchical parent weight ($w_i = 5$) significantly degrades both geometric stability (PJDD) and structural consistency (GSD). All variants are evaluated on the DT4D dataset.

Model	PJDD ↓	GSD ↓
Default	0.68	0.056
w/o. $\mathcal{L}_{\text{token}}$	1.20	0.047
w/o. $\mathcal{L}_{\text{geom}}$	1.38	0.067
w/o. $w_i = 5$	1.36	0.073

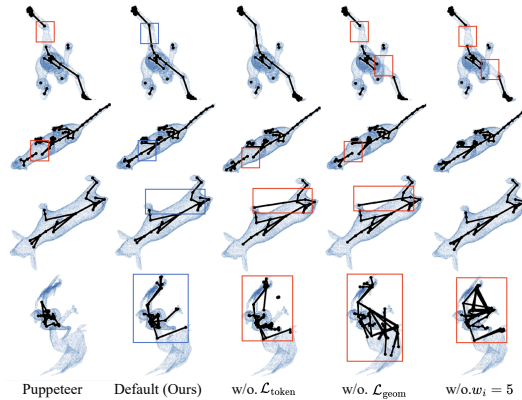


Fig. 6: Qualitative skeleton ablations. Removing $\mathcal{L}_{\text{token}}$ often omits critical limbs; removing $w_i = 5$ breaks hierarchical connectivity, causing chaotic structures; and omitting $\mathcal{L}_{\text{geom}}$ results in poor geometric alignment. Our default model consistently recovers complete skeletons.”

taining superior structural consistency (GSD). Importantly, this substantial improvement in temporal stability does not compromise per-frame fidelity; as reported in Tab. 2, SPRig preserves and even improves baseline static quality on all evaluated datasets, demonstrating strong out-of-domain generalization. Besides, our visual results (Fig. 4 and Fig. 5) show that SPRig effectively eliminates missing joints and severe inter-frame flicker, producing structurally complete and

Table 4: Quantitative ablation of anchor frame. Comparing the first frame ($c = 1$) with our automatic discovery ($c = \arg \max_k \mathcal{A}$), our approach improves both skeleton and skinning metrics on the DT4D dataset.

Metric	$c = 1$	Default
Skeleton Generation		
PJDD ↓	0.68	0.59
GSD ↓	0.056	0.046
CD-B2B ↓	0.0188	0.0175
Skinning Generation		
L_1 Error ↓	1001.56	982.35
LBS RMSE ↓	0.007558	0.007552

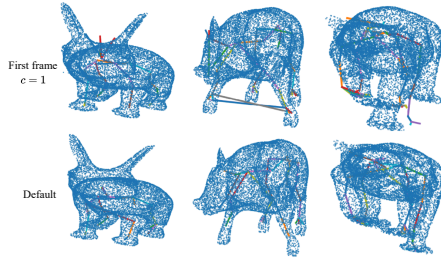


Fig. 7: Qualitative ablation of anchor frame. Conventional first frame ($c=1$) fails on severe initial self-occlusions (e.g., squatted poses), yielding corrupted skeletons. Our dynamic selection ($c = \arg \max_k \mathcal{A}$) automatically identifies the optimal rest pose for clean rigging.

smoothly moving rigs across highly diverse sequences. This reinforces our conclusion that grounding the generation process to a canonical anchor enables the model to internalize a robust, pose-invariant structural prior.

Ablations. We ablate key components of our dual-consistency training objective (see Tab. 3) and the parent-token weighting strategy ($w_i = 5$ in Sec. 4.2). Removing either the geometry-space loss or the token-space loss substantially worsens temporal stability, confirming that both constraints are critical. Similarly, reverting to standard cross-entropy (with all $w_i = 1$) by removing the parent-token weighting also degrades stability, highlighting that emphasizing root tokens is essential for stabilizing skeleton topology and reducing geometric jitter. Additionally, we assess the effect of our dynamic anchor selection (see Tab. 4, Top, and Fig. 7): automatically identifying the optimal rest pose, instead of defaulting to the first frame, is crucial for preventing initial topological corruption and further reducing geometric jitter.

6.2 Skinning Generation

Metrics. Similar to the skeleton evaluation, we report both dynamic and static metrics: (1) **Temporal L_1 Error:** Unlike VIBE’s [32] acceleration error, which measures second-order joint acceleration, we compute the first-order variation of skinning weights to directly capture temporal flicker and inconsistencies in predicted attachments across frames (see Suppl. for details). (2) **LBS RMSE:** Measures the accuracy of static surface deformation. We drive the canonical mesh using the predicted rigs via standard Linear Blend Skinning [46] and compute the vertex-wise reconstruction error against the ground truth. (3) **Precision, Recall, and Avg. L_1 Dist.** [81]: Standard metrics for static prediction quality. To verify out-of-domain single-frame robustness, these metrics are also evaluated on Articulation-XL 2.0 [68], ModelsResource [81], and the challenging Diverse-pose [65] datasets.

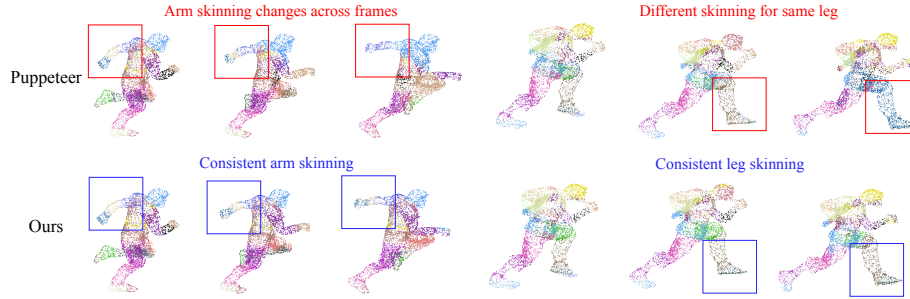


Fig. 8: Skinning qualitative comparisons. Results on running human sequences from DT4D are visualized, with each vertex colored by the joint with the maximum predicted skinning influence. Our method produces temporally consistent assignments for arms and legs across frames (blue boxes), whereas Puppeteer shows severe flickering, with dominant joint assignments switching between frames (red boxes).

Results. Our method (see Tab. 1, Right) significantly reduces the temporal L_1 error compared to the static baselines, demonstrating that our fine-tuning effectively mitigates inter-frame flicker in skinning assignments. At the same time, the LBS RMSE is consistently improved over both baselines, indicating that the substantial gains in temporal stability do not compromise—and in fact enhance—the deformation fidelity for skinning generation. Moreover, our fine-tuning strategy maintains competitive performance on out-of-domain static datasets (see Tab. 5) and even surpasses all baselines on the Diverse-Pose challenge dataset. Visually, our method (see Figs. 8 and 9) produces highly consistent vertex-to-joint skinning attachments across frames and effectively suppresses per-vertex temporal deviations.

Table 5: Skinning static prediction comparisons. Our method achieves competitive per-frame fidelity on Articulation-XL 2.0 and ModelsResource, while consistently outperforming the baseline on the challenging Diverse-pose dataset, demonstrating greater robustness to extreme articulations.

Model	Articulation-XL 2.0			ModelsResource			Diverse-Pose		
	Precision \uparrow	Recall \uparrow	Avg. L_1 Dist. \downarrow	Precision \uparrow	Recall \uparrow	Avg. L_1 Dist. \downarrow	Precision \uparrow	Recall \uparrow	Avg. L_1 Dist. \downarrow
RigNet	0.737	0.661	0.729	0.657	0.802	0.707	0.747	0.654	0.746
Puppeteer	0.876	0.740	0.335	0.797	0.816	0.443	0.836	0.722	0.405
Ours	0.863	0.745	0.355	0.732	0.883	0.462	0.842	0.734	0.378

Ablations. To validate the necessity of each component in our skinning loss, we perform an ablation study (see Tab. 6) by removing individual terms while keeping other settings fixed. All model variants converge within ~ 10 epochs, but removing the distillation terms or regularizers significantly degrades temporal stability and deformation fidelity. Qualitative results (see Figs. 10 and 11) show these components are critical for stable, sharp skinning assignments. Removing



Fig. 9: Temporally consistent skinning. We visualize per-vertex inconsistencies between perturbed-frame skinning predictions and the canonical anchor teacher using the L_1 deviation of predicted weights (blue: low error; red: high error). Puppeteer (Left) exhibits large high-error regions, indicating strong temporal flicker, whereas our method (Right) largely suppresses these errors, consistent with the results in Tab. 1, Right. Additional discussion is provided in the Supplement.

Table 6: Quantitative skinning ablations. Removing any loss term significantly degrades temporal stability (L_1 Error) and fidelity (LBS RMSE). Models trained for 24 epochs. All variants are evaluated on the DT4D dataset.

Model	L_1 Error \downarrow	LBS RMSE \downarrow
Default	982.35	0.007552
w/o. \mathcal{L}_{sym}	3897.24	0.016587
w/o. \mathcal{L}_1	4007.13	0.023254
w/o. $\mathcal{L}_{\text{anchor}}$	4006.53	0.023305
w/o. \mathcal{L}_{ent}	4007.74	0.023311
w/o. $\mathcal{L}_{\text{prior}}$	4006.78	0.023347

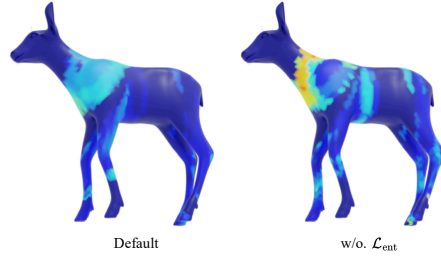


Fig. 10: Qualitative \mathcal{L}_{ent} ablation. Per-vertex Shannon entropy is visualized (blue: sharp; red: diffuse). Our full model (Left) produces sparse, confident assignments, whereas removing \mathcal{L}_{ent} yields ambiguous weights, reducing stability.



Fig. 11: Qualitative skinning ablations. Removing the symmetry loss \mathcal{L}_{sym} causes weight leakage and violates anatomical structure. Omitting the geometric prior $\mathcal{L}_{\text{prior}}$ or entropy loss \mathcal{L}_{ent} produces diffuse, low-confidence weights. Our full model yields sharp, localized, and structurally sound skinning, matching or surpassing the pretrained Puppeteer.

the symmetry loss \mathcal{L}_{sym} (Eq. (8)) causes severe weight leakage, while omitting the geometric prior $\mathcal{L}_{\text{prior}}$ (Eq. (12)) or entropy loss \mathcal{L}_{ent} (Eq. (11)) produces diffuse, low-confidence weights. We highlight that the entropy regularization (see Fig. 10) further encourages sparse, confident assignments; without \mathcal{L}_{ent} , weights become ambiguous, reducing stability. We also validate that our automatic anchor frame strategy improves skinning weight generation (see Tab. 4, Bottom), outperforming the naive approach of setting $c = 1$.

7 Discussion

Our work introduces a new perspective on automatic data-driven model rigging by leveraging self-supervised unlabeled dynamic mesh sequences. We propose a general fine-tuning framework that addresses severe temporal inconsistencies in SOTA static rigging models applied to animated sequences. Extensive experiments show that our method achieves superior temporal stability on both skeleton and skinning generation tasks, while maintaining or even improving the model’s original static generation quality. We hope this work serves as a first step toward deformation-driven rigging and inspires further research in this direction.

Future work. Our framework opens several research directions, such as fine-tuning on longer mesh sequences to capture complex dynamics and improve long-term temporal consistency.

References

1. Amenta, N., Bern, M.: Surface reconstruction by voronoi filtering. In: Proceedings of the fourteenth annual symposium on Computational geometry. pp. 39–48 (1998)
2. Anguelov, D., Srinivasan, P., Koller, D., Thrun, S., Rodgers, J., Davis, J.: Scape: shape completion and animation of people. In: ACM Siggraph 2005 Papers, pp. 408–416 (2005)
3. Au, O.K.C., Tai, C.L., Chu, H.K., Cohen-Or, D., Lee, T.Y.: Skeleton extraction by mesh contraction. *ACM transactions on graphics (TOG)* **27**(3), 1–10 (2008)
4. Baran, I., Popović, J.: Automatic rigging and animation of 3d characters. *ACM Transactions on graphics (TOG)* **26**(3), 72–es (2007)
5. Bengio, S., Vinyals, O., Jaitly, N., Shazeer, N.: Scheduled sampling for sequence prediction with recurrent neural networks. *Advances in neural information processing systems* **28** (2015)
6. Bhati, Z., Shah, A., Waqas, A., Malik, H.A.M.: Template based procedural rigging of quadrupeds with custom manipulators. In: 2013 International Conference on Advanced Computer Science Applications and Technologies. pp. 259–264. IEEE (2013)
7. Bian, S., Zheng, A., Chaudhry, E., You, L., Zhang, J.J.: Automatic generation of dynamic skin deformation for animated characters. *Symmetry* **10**(4), 89 (2018)
8. Bogo, F., Romero, J., Pons-Moll, G., Black, M.J.: Dynamic faust: Registering human bodies in motion. In: Proceedings of the IEEE conference on computer vision and pattern recognition. pp. 6233–6242 (2017)
9. Cao, J., Tagliasacchi, A., Olson, M., Zhang, H., Su, Z.: Point cloud skeletons via laplacian based contraction. In: 2010 Shape Modeling International Conference. pp. 187–197. IEEE (2010)
10. Chadwick, J.E., Haumann, D.R., Parent, R.E.: Layered construction for deformable animated characters. *ACM Siggraph Computer Graphics* **23**(3), 243–252 (1989)
11. Chen, C., Huang, S., Chen, X., Chen, G., Han, X., Zhang, K., Gong, M.: Ct4d: Consistent text-to-4d generation with animatable meshes. *arXiv preprint arXiv:2408.08342* (2024)
12. Chen, X., Zheng, Y., Black, M.J., Hilliges, O., Geiger, A.: Snarf: Differentiable forward skinning for animating non-rigid neural implicit shapes. In: Proceedings of the IEEE/CVF International Conference on Computer Vision. pp. 11594–11604 (2021)

13. Chu, Z., Xiong, F., Liu, M., Zhang, J., Shao, M., Sun, Z., Wang, D., Xu, M.: Humanrig: Learning automatic rigging for humanoid character in a large scale dataset. In: Proceedings of the Computer Vision and Pattern Recognition Conference. pp. 304–313 (2025)
14. Chung, F.R.: Spectral graph theory, vol. 92. American Mathematical Soc. (1997)
15. Collet, A., Chuang, M., Sweeney, P., Gillett, D., Evseev, D., Calabrese, D., Hoppe, H., Kirk, A., Sullivan, S.: High-quality streamable free-viewpoint video. *ACM Transactions on Graphics (ToG)* **34**(4), 1–13 (2015)
16. De Aguiar, E., Theobalt, C., Thrun, S., Seidel, H.P.: Automatic conversion of mesh animations into skeleton-based animations. In: *Computer Graphics Forum*. vol. 27, pp. 389–397. Wiley Online Library (2008)
17. Deitke, M., Liu, R., Wallingford, M., Ngo, H., Michel, O., Kusupati, A., Fan, A., Laforte, C., Voleti, V., Gadre, S.Y., Vanderbilt, E., Kembhavi, A., Vondrick, C., Gkioxari, G., Ehsani, K., Schmidt, L., Farhadi, A.: Objaverse-xl: A universe of 10m+ 3d objects. arXiv preprint arXiv:2307.05663 (2023)
18. Deitke, M., Liu, R., Wallingford, M., Ngo, H., Michel, O., Kusupati, A., Fan, A., Laforte, C., Voleti, V., Gadre, S.Y., et al.: Objaverse-xl: A universe of 10m+ 3d objects. *Advances in Neural Information Processing Systems* **36**, 35799–35813 (2023)
19. Deitke, M., Schwenk, D., Salvador, J., Weihs, L., Michel, O., Vanderbilt, E., Schmidt, L., Ehsani, K., Kembhavi, A., Farhadi, A.: Objaverse: A universe of annotated 3d objects. In: Proceedings of the IEEE/CVF Conference on Computer Vision and Pattern Recognition. pp. 13142–13153 (2023)
20. Deitke, M., Schwenk, D., Salvador, J., Weihs, L., Michel, O., Vanderbilt, E., Schmidt, L., Ehsani, K., Kembhavi, A., Farhadi, A.: Objaverse: A universe of annotated 3d objects. In: Proceedings of the IEEE/CVF conference on computer vision and pattern recognition. pp. 13142–13153 (2023)
21. Feng, A., Casas, D., Shapiro, A.: Avatar reshaping and automatic rigging using a deformable model. In: Proceedings of the 8th ACM SIGGRAPH Conference on Motion in Games. pp. 57–64 (2015)
22. Goel, S., Pavlakos, G., Rajasegaran, J., Kanazawa, A., Malik, J.: Humans in 4d: Reconstructing and tracking humans with transformers. In: Proceedings of the IEEE/CVF International Conference on Computer Vision. pp. 14783–14794 (2023)
23. Gottschalk, S., Lin, M.C., Manocha, D.: Obbtrees: A hierarchical structure for rapid interference detection. In: Proceedings of the 23rd annual conference on Computer graphics and interactive techniques. pp. 171–180 (1996)
24. Guo, Z., Xiang, J., Ma, K., Zhou, W., Li, H., Zhang, R.: Make-it-animatable: An efficient framework for authoring animation-ready 3d characters. In: Proceedings of the Computer Vision and Pattern Recognition Conference. pp. 10783–10792 (2025)
25. He, G., Geng, C., Wu, S., Wu, J.: Category-agnostic neural object rigging. In: Proceedings of the Computer Vision and Pattern Recognition Conference. pp. 22078–22088 (2025)
26. Hinton, G., Vinyals, O., Dean, J.: Distilling the knowledge in a neural network. arXiv preprint arXiv:1503.02531 (2015)
27. James, D.L., Twigg, C.D.: Skinning mesh animations. *ACM Transactions on Graphics (TOG)* **24**(3), 399–407 (2005)
28. Jin, X., Kim, J.: A 3d skeletonization algorithm for 3d mesh models using a partial parallel 3d thinning algorithm and 3d skeleton correcting algorithm. *Applied Sciences* **7**(2), 139 (2017)
29. Joshi, P., Meyer, M., DeRose, T., Green, B., Sanocki, T.: Harmonic coordinates for character articulation. *ACM transactions on graphics (TOG)* **26**(3), 71–es (2007)

30. Kavan, L., Collins, S., Žára, J., O’Sullivan, C.: Skinning with dual quaternions. In: Proceedings of the 2007 symposium on Interactive 3D graphics and games. pp. 39–46 (2007)
31. Kavan, L., Sloan, P.P., O’Sullivan, C.: Fast and efficient skinning of animated meshes. In: Computer Graphics Forum. vol. 29, pp. 327–336. Wiley Online Library (2010)
32. Kocabas, M., Athanasiou, N., Black, M.J.: Vibe: Video inference for human body pose and shape estimation. In: Proceedings of the IEEE/CVF conference on computer vision and pattern recognition. pp. 5253–5263 (2020)
33. Kullback, S., Leibler, R.A.: On information and sufficiency. *The annals of mathematical statistics* **22**(1), 79–86 (1951)
34. Le, B.H., Deng, Z.: Robust and accurate skeletal rigging from mesh sequences. *ACM Transactions on Graphics (TOG)* **33**(4), 1–10 (2014)
35. LeCun, Y., Bengio, Y., Hinton, G.: Deep learning. *nature* **521**(7553), 436–444 (2015)
36. Lewis, J.P., Corder, M., Fong, N.: Pose space deformation: a unified approach to shape interpolation and skeleton-driven deformation. In: *Seminal Graphics Papers: Pushing the Boundaries, Volume 2*, pp. 811–818 (2023)
37. Li, P., Aberman, K., Hanocka, R., Liu, L., Sorkine-Hornung, O., Chen, B.: Learning skeletal articulations with neural blend shapes. *ACM Transactions on Graphics (TOG)* **40**(4), 1–15 (2021)
38. Li, Y., Takehara, H., Taketomi, T., Zheng, B., Nießner, M.: 4dcomplete: Non-rigid motion estimation beyond the observable surface. In: Proceedings of the IEEE/CVF International Conference on Computer Vision. pp. 12706–12716 (2021)
39. Lin, C., Liu, H., Lin, Q., Bright, Z., Tang, S., He, Y., Liu, M., Zhu, L., Le, C.: Objaverse++: Curated 3d object dataset with quality annotations. *arXiv preprint arXiv:2504.07334* (2025)
40. Lin, K., Wang, L., Liu, Z.: End-to-end human pose and mesh reconstruction with transformers. In: Proceedings of the IEEE/CVF conference on computer vision and pattern recognition. pp. 1954–1963 (2021)
41. Liu, I., Xu, Z., Yifan, W., Tan, H., Xu, Z., Wang, X., Su, H., Shi, Z.: Riganything: Template-free autoregressive rigging for diverse 3d assets. *ACM Transactions on Graphics (TOG)* **44**(4), 1–12 (2025)
42. Liu, L., Zheng, Y., Tang, D., Yuan, Y., Fan, C., Zhou, K.: Neuroskinning: Automatic skin binding for production characters with deep graph networks. *ACM Transactions on Graphics (ToG)* **38**(4), 1–12 (2019)
43. Loshchilov, I., Hutter, F.: Decoupled weight decay regularization. In: *International Conference on Learning Representations* (2017)
44. Ma, J., Zhang, D.: Tarig: Adaptive template-aware neural rigging for humanoid characters. *Computers & Graphics* **114**, 158–167 (2023)
45. Ma, Q., Yang, J., Ranjan, A., Pujades, S., Pons-Moll, G., Tang, S., Black, M.J.: Learning to Dress 3D People in Generative Clothing. In: *Computer Vision and Pattern Recognition (CVPR)* (2020)
46. Magnenat-Thalmann, N., Laperrière, R., Thalmann, D.: Joint-dependent local deformations for hand animation and object grasping. In: *Proceedings on Graphics interface’88*. pp. 26–33 (1989)
47. Mamou, K., Zaharia, T., Prêteux, F.: A skinning approach for dynamic 3d mesh compression. *Computer Animation and Virtual Worlds* **17**(3-4), 337–346 (2006)
48. Marr, D., Nishihara, H.K.: Representation and recognition of the spatial organization of three-dimensional shapes. *Proceedings of the Royal Society of London. Series B. Biological Sciences* **200**(1140), 269–294 (1978)

49. Micikevicius, P., Narang, S., Alben, J., Diamos, G., Elsen, E., Garcia, D., Ginsburg, B., Houston, M., Kuchaiev, O., Venkatesh, G., et al.: Mixed precision training. In: International Conference on Learning Representations (2018)
50. Moutafidou, A., Toulatzis, V., Fudos, I.: Deep fusible skinning of animation sequences. *The Visual Computer* **40**(8), 5695–5715 (2024)
51. Orvalho, V.C., Zacur, E., Susin, A.: Transferring the rig and animations from a character to different face models. In: *Computer Graphics Forum*. vol. 27, pp. 1997–2012. Wiley Online Library (2008)
52. Osada, R., Funkhouser, T., Chazelle, B., Dobkin, D.: Shape distributions. *ACM Transactions on Graphics (TOG)* **21**(4), 807–832 (2002)
53. Pan, J., Yang, X., Xie, X., Willis, P., Zhang, J.J.: Automatic rigging for animation characters with 3d silhouette. *Computer Animation and Virtual Worlds* **20**(2-3), 121–131 (2009)
54. Pan, X., Huang, J., Mai, J., Wang, H., Li, H., Su, T., Wang, W., Jin, X.: Heter-skinnet: A heterogeneous network for skin weights prediction. In: *Proceedings of the ACM on computer graphics and interactive techniques*. vol. 4. Association for Computing Machinery (2021)
55. Pantuwong, N., Sugimoto, M.: A fully automatic rigging algorithm for 3d character animation. In: *SIGGRAPH Asia 2011 Posters*, pp. 1–1 (2011)
56. Pantuwong, N., Sugimoto, M.: A novel template-based automatic rigging algorithm for articulated-character animation. *Computer Animation and Virtual Worlds* **23**(2), 125–141 (2012)
57. Park, C., Jeong, Y., Cho, M., Park, J.: Fast point transformer. In: *Proceedings of the IEEE/CVF conference on computer vision and pattern recognition*. pp. 16949–16958 (2022)
58. Paszke, A., Gross, S., Massa, F., Lerer, A., Bradbury, J., Chanan, G., Killeen, T., Lin, Z., Gimelshein, N., Antiga, L., et al.: Pytorch: An imperative style, high-performance deep learning library. *Advances in neural information processing systems* **32** (2019)
59. Pavllo, D., Feichtenhofer, C., Grangier, D., Auli, M.: 3d human pose estimation in video with temporal convolutions and semi-supervised training. In: *Proceedings of the IEEE/CVF conference on computer vision and pattern recognition*. pp. 7753–7762 (2019)
60. Radford, A., Narasimhan, K., Salimans, T., Sutskever, I., et al.: Improving language understanding by generative pre-training (2018)
61. Ranzato, M., Chopra, S., Auli, M., Zaremba, W.: Sequence level training with recurrent neural networks. *arXiv preprint arXiv:1511.06732* (2015)
62. Sabathier, R., Mitra, N.J., Novotny, D.: Animal avatars: Reconstructing animatable 3d animals from casual videos. In: *European Conference on Computer Vision*. pp. 270–287. Springer (2024)
63. Shannon, C.E.: A mathematical theory of communication. *The Bell system technical journal* **27**(3), 379–423 (1948)
64. Shi, Y., Liu, Y., Wu, Y., Liu, X., Zhao, C., Luo, J., Zhou, B.: Drive any mesh: 4d latent diffusion for mesh deformation from video. *arXiv preprint arXiv:2506.07489* (2025)
65. Song, C., Li, X., Yang, F., Xu, Z., Wei, J., Liu, F., Feng, J., Lin, G., Zhang, J.: Puppeteer: Rig and animate your 3d models. *arXiv preprint arXiv:2508.10898* (2025)
66. Song, C., Wei, J., Chen, T., Chen, Y., Foo, C.S., Liu, F., Lin, G.: Moda: Modeling deformable 3d objects from casual videos. *International Journal of Computer Vision* **133**(5), 2825–2844 (2025)

67. Song, C., Wei, J., Foo, C.S., Lin, G., Liu, F.: Reacto: Reconstructing articulated objects from a single video. In: Proceedings of the IEEE/CVF Conference on Computer Vision and Pattern Recognition. pp. 5384–5395 (2024)
68. Song, C., Zhang, J., Li, X., Yang, F., Chen, Y., Xu, Z., Liew, J.H., Guo, X., Liu, F., Feng, J., et al.: Magicarticulate: Make your 3d models articulation-ready. In: Proceedings of the Computer Vision and Pattern Recognition Conference. pp. 15998–16007 (2025)
69. Sun, K., Litvak, D., Zhang, Y., Li, H., Wu, J., Wu, S.: Ponymation: Learning articulated 3d animal motions from unlabeled online videos. In: European Conference on Computer Vision. pp. 100–119. Springer (2024)
70. Sun, M., Chen, J., Dong, J., Chen, Y., Jiang, X., Mao, S., Jiang, P., Wang, J., Dai, B., Huang, R.: Drive: Diffusion-based rigging empowers generation of versatile and expressive characters. In: Proceedings of the Computer Vision and Pattern Recognition Conference. pp. 21170–21180 (2025)
71. Sun, M., Mao, S., Chen, K., Chen, Y., Lu, S., Wang, J., Dong, J., Huang, R.: Armo: Autoregressive rigging for multi-category objects. arXiv preprint arXiv:2503.20663 (2025)
72. Tagliasacchi, A., Alhashim, I., Olson, M., Zhang, H.: Mean curvature skeletons. In: Computer Graphics Forum. vol. 31, pp. 1735–1744. Wiley Online Library (2012)
73. Tagliasacchi, A., Zhang, H., Cohen-Or, D.: Curve skeleton extraction from incomplete point cloud. In: ACM SIGGRAPH 2009 papers, pp. 1–9 (2009)
74. Umeyama, S.: Least-squares estimation of transformation parameters between two point patterns. IEEE Transactions on pattern analysis and machine intelligence **13**(4), 376–380 (2002)
75. Vaswani, A., Shazeer, N., Parmar, N., Uszkoreit, J., Jones, L., Gomez, A.N., Kaiser, Ł., Polosukhin, I.: Attention is all you need. Advances in neural information processing systems **30** (2017)
76. Wang, M., Yan, Q., Cao, Z., Li, Y., Mac Aodha, O., Corso, J.J., Vaxman, A.: Bimotion: B-spline motion for text-guided dynamic 3d character generation. In: Proceedings of the IEEE/CVF Conference on Computer Vision and Pattern Recognition (CVPR) (2026)
77. Williams, R.J., Zipser, D.: A learning algorithm for continually running fully recurrent neural networks. Neural computation **1**(2), 270–280 (1989)
78. Wu, S., Li, R., Jakab, T., Rupprecht, C., Vedaldi, A.: Magicpony: Learning articulated 3d animals in the wild. In: Proceedings of the IEEE/CVF Conference on Computer Vision and Pattern Recognition. pp. 8792–8802 (2023)
79. Wu, X., Jiang, L., Wang, P.S., Liu, Z., Liu, X., Qiao, Y., Ouyang, W., He, T., Zhao, H.: Point transformer v3: Simpler faster stronger. In: Proceedings of the IEEE/CVF conference on computer vision and pattern recognition. pp. 4840–4851 (2024)
80. Wu, Z., Yu, C., Wang, F., Bai, X.: Animateanymesh: A feed-forward 4d foundation model for text-driven universal mesh animation. arXiv preprint arXiv:2506.09982 (2025)
81. Xu, Z., Zhou, Y., Kalogerakis, E., Landreth, C., Singh, K.: Rignet: neural rigging for articulated characters. ACM Transactions on Graphics (TOG) **39**(4), 58–1 (2020)
82. Xu, Z., Zhou, Y., Yi, L., Kalogerakis, E.: Morig: Motion-aware rigging of character meshes from point clouds. In: SIGGRAPH Asia 2022 conference papers. pp. 1–9 (2022)

83. Yan, Y., Letscher, D., Ju, T.: Voxel cores: Efficient, robust, and provably good approximation of 3d medial axes. *ACM Transactions on Graphics (TOG)* **37**(4), 1–13 (2018)
84. Yan, Y., Sykes, K., Chambers, E., Letscher, D., Ju, T.: Erosion thickness on medial axes of 3d shapes. *ACM Transactions on Graphics (TOG)* **35**(4), 1–12 (2016)
85. Yang, G., Sun, D., Jampani, V., Vlasic, D., Cole, F., Chang, H., Ramanan, D., Freeman, W.T., Liu, C.: Lasr: Learning articulated shape reconstruction from a monocular video. In: *Proceedings of the IEEE/CVF Conference on Computer Vision and Pattern Recognition*. pp. 15980–15989 (2021)
86. Yang, G., Vo, M., Neverova, N., Ramanan, D., Vedaldi, A., Joo, H.: Banmo: Building animatable 3d neural models from many casual videos. In: *Proceedings of the IEEE/CVF Conference on Computer Vision and Pattern Recognition*. pp. 2863–2873 (2022)
87. Yao, Y., Deng, Z., Hou, J.: Riggs: Rigging of 3d gaussians for modeling articulated objects in videos. In: *Proceedings of the Computer Vision and Pattern Recognition Conference*. pp. 5592–5601 (2025)
88. Yoo, J., Kim, H.: A comprehensive pipeline for large-scale 3d humanoid rigging dataset creation. *TECHART: Journal of Arts and Imaging Science* **12**(3), 54–60 (2025)
89. Yu, X., Tang, L., Rao, Y., Huang, T., Zhou, J., Lu, J.: Point-bert: Pre-training 3d point cloud transformers with masked point modeling. In: *Proceedings of the IEEE/CVF conference on computer vision and pattern recognition*. pp. 19313–19322 (2022)
90. Yuan, Y.J., Kobbelt, L., Liu, J., Zhang, Y., Wan, P., Lai, Y.K., Gao, L.: 4dynamic: Text-to-4d generation with hybrid priors. *CoRR* (2024)
91. Zeng, C., Dong, Y., Peers, P., Wu, H., Tong, X.: Renderformer: Transformer-based neural rendering of triangle meshes with global illumination. In: *Proceedings of the Special Interest Group on Computer Graphics and Interactive Techniques Conference Conference Papers*. pp. 1–11 (2025)
92. Zhang, C., Wan, H., Shen, X., Wu, Z.: Patchformer: An efficient point transformer with patch attention. In: *Proceedings of the IEEE/CVF conference on computer vision and pattern recognition*. pp. 11799–11808 (2022)
93. Zhang, H., Chang, D., Li, F., Soleymani, M., Ahuja, N.: Magicpose4d: Crafting articulated models with appearance and motion control. *arXiv preprint arXiv:2405.14017* (2024)
94. Zhang, J.P., Pu, C.F., Guo, M.H., Cao, Y.P., Hu, S.M.: One model to rig them all: Diverse skeleton rigging with unrig. *ACM Transactions on Graphics (TOG)* **44**(4), 1–18 (2025)
95. Zhang, J.p., Pu, C.F., Guo, M.H., Cao, Y.P., Hu, S.M.: Skin tokens: A learned compact representation for unified autoregressive rigging. *arXiv preprint arXiv:2602.04805* (2026)
96. Zhang, Y., Zhang, L., Ma, R., Cao, N.: Texverse: A universe of 3d objects with high-resolution textures. *arXiv preprint arXiv:2508.10868* (2025)
97. Zhao, H., Jiang, L., Jia, J., Torr, P.H., Koltun, V.: Point transformer. In: *Proceedings of the IEEE/CVF international conference on computer vision*. pp. 16259–16268 (2021)
98. Zheng, C., Mendieta, M., Wang, P., Lu, A., Chen, C.: A lightweight graph transformer network for human mesh reconstruction from 2d human pose. In: *Proceedings of the 30th ACM international conference on multimedia*. pp. 5496–5507 (2022)

99. Zhong, S., Peng, J., Zheng, Z., Huang, Z., Ma, W., Zhang, G., Liu, Q., Yuille, A., Chen, J.: 4d-animal: Freely reconstructing animatable 3d animals from videos. arXiv preprint arXiv:2507.10437 (2025)

SPRig: Self-Supervised Pose-Invariant Rigging from Dynamic Mesh Sequences

Supplementary Material

A Evaluation Details: LBS RMSE Computation

Evaluating the LBS RMSE requires per-bone transformations for every frame. Since our framework outputs a pose-invariant static rig (canonical skeleton and skinning weights) without explicit temporal kinematics, we derive the per-frame joint transformations via a differentiable pose fitting procedure.

Specifically, given the canonical mesh vertices V_{rest} , the predicted skeleton, and the pose-invariant skinning weights W , we optimize the local joint rotations (parameterized as axis-angles) and translations for each frame t . The objective is to minimize the pointwise L_2 distance between the LBS-driven vertices \hat{V}_t and the ground-truth target mesh vertices V_t .

For computational efficiency, we randomly sample 5,000 vertices per frame to compute the loss. The optimization is solved using the Adam optimizer with a learning rate of 0.01 for 60 iterations per frame. To maintain temporal coherence and accelerate convergence, we employ a warm-start strategy: the kinematic parameters optimized for frame $t-1$ are used as the initialization for frame t . The final LBS RMSE is then computed across all vertices using these optimally fitted transformations, ensuring the metric strictly reflects the deformation fidelity of the predicted rigs.

B Robustness to Extreme Poses and Self-Occlusions

To demonstrate that SPRig learns a generalizable, pose-invariant structural prior rather than trivially memorizing a sequence-specific anchor, we provide qualitative results on challenging out-of-domain static meshes.

As shown in Fig. 1, the baseline (Puppeteer) frequently drops fine-grained distal structures (e.g., individual fingers) under severe self-occlusions. Static models rely heavily on superficial spatial features, which easily collapse when extremities are curled or heavily deformed.

In contrast, SPRig robustly infers topologically complete skeletons from single, heavily deformed meshes. By enforcing consistency across dynamic frames, where complex structures transition between extended and occluded states, SPRig explicitly learns the underlying *kinematic invariance*. It internalizes that intrinsic skeletal topology persists regardless of severe spatial deformations. This confirms that our framework endows the network with a robust structural prior, enabling superior out-of-domain generalization that extends far beyond simple temporal post-processing.

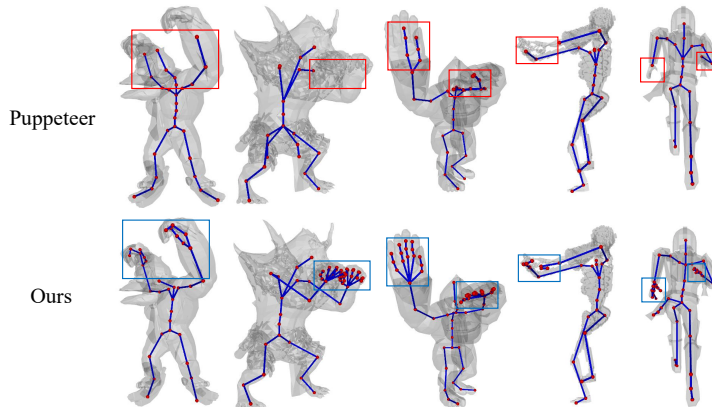


Fig. 1: Robustness to extreme poses and self-occlusions. Qualitative comparison between Puppeteer (top) and our SPRig (bottom) on highly articulated character meshes. In challenging poses or under severe self-occlusion, the baseline model frequently drops fine-grained extremities (e.g., missing hand and finger rigs, highlighted in red boxes) because it relies heavily on superficial geometric cues. In contrast, by learning the kinematic invariance of structures during dynamic sequence fine-tuning, SPRig internalizes a robust pose-invariant prior. This enables it to preserve complete, highly detailed skeletal topologies (e.g., full five-finger structures, highlighted in blue boxes) even from single, heavily deformed inputs, demonstrating superior out-of-domain generalization.

C Failure Cases and Limitations: Symmetric Ambiguity

While SPRig significantly improves topological stability and out-of-domain generalization, it can occasionally fail under extreme spatial entanglement—a limitation primarily inherited from the geometric feature extraction mechanism of the underlying static foundation model.

As illustrated in Fig. 2, when symmetric or distinct body parts (e.g., left and right hands, or hands resting on legs) are in extremely close physical proximity during complex interactions, the model suffers from *symmetric ambiguity*. Because the point-cloud encoder of the baseline model aggregates features based on spatial (Euclidean) proximity rather than intrinsic surface geodesics, the geometric signatures of physically touching parts become highly entangled. Consequently, when the autoregressive decoder interprets these entangled features, it is prone to predicting an incorrect **parent token** ($t_{j,p}$) for the affected joint. Instead of connecting to its true anatomical parent, the joint is erroneously parented to a spatially adjacent but kinematically distant cluster, generating a spurious "long bone" artifact bridging the gap.

Crucially, if such severe spatial entanglement persists even in our automatically selected canonical anchor frame, SPRig’s strict consistency mechanism will faithfully—yet incorrectly—propagate this erroneous parent token across the entire sequence. Addressing this limitation is an important direction for future

work. Potential solutions include replacing Euclidean-based feature aggregation with geodesic distance metrics (which respect surface topology) or incorporating explicit semantic body-part priors to better disentangle spatially adjacent regions during token decoding.

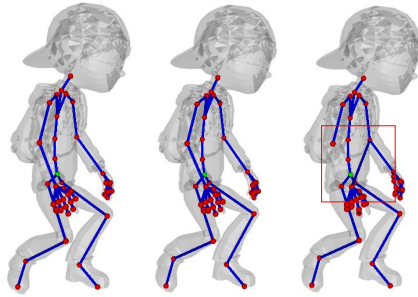


Fig. 2: Failure case: Symmetric ambiguity. During complex poses where distinct parts are in close spatial proximity, the Euclidean-based feature encoder entangles their geometric representations. This ambiguity confuses the autoregressive decoder, causing it to predict an incorrect parent token ($t_{j,p}$). As a result, a spurious connection (a "long bone" artifact highlighted in the red box) bridges kinematically distant but spatially close regions.

D Video-based Motion Fidelity on the *fish* Sequence

To quantitatively assess whether the final rig better captures motion, we run the same video-guided animation optimization with two different final rigs: (i) the original Puppeteer rig [2] and (ii) our final rig. For both methods, we compare the reconstructed front-view video against the ground-truth driving video. The two videos are first aligned over their common temporal duration, resampled to 10 FPS, and resized to a width of 256 while preserving aspect ratio. The video is attached in the video folder.

We report frame-wise appearance metrics, including L1, PSNR, and SSIM [3], together with two motion-sensitive measures computed from consecutive frames. Specifically, *Temporal-L1* measures the discrepancy between frame-to-frame RGB changes, while *Flow-EPE_{norm}* measures the normalized endpoint error between dense Farneback optical flow fields [1].

As shown in Table 1, our method achieves consistent improvements over Puppeteer on the *fish* sequence. In particular, our rig produces lower L1 error (0.147630 vs. 0.147960), higher PSNR (10.704060 vs. 10.693136), and higher SSIM (0.686730 vs. 0.686409). More importantly, it also yields lower temporal discrepancy and lower flow error, with Temporal-L1 reduced from 0.023395 to 0.023275 and normalized Flow-EPE reduced from 0.002342 to 0.002322. These

Method	L1↓	PSNR↑	SSIM↑	Temporal-L1↓	Flow-EPE _{norm} ↓
Puppeteer	0.147960	10.693136	0.686409	0.023395	0.002342
Ours	0.147630	10.704060	0.686730	0.023275	0.002322

Table 1: Video-based motion fidelity evaluation on the reconstructed front-view video for the *fish* sequence. Lower is better except for PSNR and SSIM.

results suggest that our final rig provides a slightly better basis for reconstructing the target motion on this example.

References

1. Farnebäck, G.: Two-frame motion estimation based on polynomial expansion. In: Scandinavian conference on Image analysis. pp. 363–370. Springer (2003)
2. Song, C., Li, X., Yang, F., Xu, Z., Wei, J., Liu, F., Feng, J., Lin, G., Zhang, J.: Puppeteer: Rig and animate your 3d models. arXiv preprint arXiv:2508.10898 (2025)
3. Wang, Z., Bovik, A.C., Sheikh, H.R., Simoncelli, E.P.: Image quality assessment: from error visibility to structural similarity. *IEEE transactions on image processing* **13**(4), 600–612 (2004)